Journal of Materials Chemistry A

PAPER

View Article Online
View Journal | View Issue

Cite this: J. Mater. Chem. A, 2016, 4, 2122

Cloud-like graphene nanoplatelets on $Nd_{0.5}Sr_{0.5}CoO_{3-\delta}$ nanorods as an efficient bifunctional electrocatalyst for hybrid Li–air batteries†

Changmin Kim,[a] Ohhun Gwon,[a] In-Yup Jeon,[a] Youngsik Kim,[a] Jeeyoung Shin,[b] Young-Wan Ju,*[a] Jong-Beom Baek*[a] and Guntae Kim*[a]

Received 22nd October 2015
Accepted 8th January 2016

DOI: 10.1039/c5ta08493h

www.rsc.org/MaterialsA

With the recognition of metal–air batteries as promising candidates for clean and efficient energy storage, the development of inexpensive and effective bifunctional catalysts for the oxygen reduction reaction (ORR) and the oxygen evolution reaction (OER) has become one of the most important topics in this field. Herein, we designed new composite catalysts consisting of a nanorod type $Nd_{0.5}Sr_{0.5}CoO_{3-\delta}$ (NSC) perovskite and edge-iodinated graphene nanoplatelets (IGnPs) as bifunctional catalysts for ORR and OER. Interestingly, the simple application of ultrasonication endowed the catalyst with a fascinating morphology comprising cloud-like IGnPs on NSC nanorods (NSC@IGnP). Benefiting from the unique morphological features, NSC@IGnP provides superior bifunctional activities toward both ORR and OER, remarkable cell performance, and exceptionally high stability for hybrid Li–air batteries.

Introduction

With the exponential growth of energy consumption, aprotic Li–air batteries have attracted attention because of their high theoretical energy density in comparison with that of other rechargeable batteries, such as Ni–metal hydride, Li-ion polymer, and Li–S batteries.[1–4] The practical energy density of aprotic Li–O_2 batteries, however, is hindered due to the insoluble discharge products clogging the air electrodes and the additional components required to supply pure oxygen gas.[5,6] Moreover, poor oxygen reduction reaction (ORR) and oxygen evolution reaction (OER) kinetics in the aprotic electrolyte cause a high overpotential during discharge and charge processes,[2,5] resulting in decomposition of the electrolyte with the formation of Li_2CO_3.[7] Interestingly, hybrid Li–air batteries with a solid electrolyte membrane can solve these problems by separating the Li metal anode in an organic electrolyte from the air electrode in an aqueous electrolyte. However, in spite of these design benefits, sluggish kinetics at the air electrode for the ORR and OER usually mandates the use of noble metal-based catalysts such as Pt/C and IrO_2.

In these regards, heteroatom-doped carbon-based materials, such as boron (B), nitrogen (N), phosphorus (P), and iron (Fe), have been considered as alternatives to Pt-based catalysts due to their highly catalytic properties for ORR.[8–12] Jeon *et al.*, for the first time, fabricated edge-halogenated graphene nanoplatelets (XGnPs, X = F, Cl, Br, I) *via* ball-milling graphite in the presence of fluorine, chlorine, bromine, and iodine.[13] XGnPs have favorable binding affinity with O_2 molecules and weaken O–O bond strengths of oxygen molecules as a result of the halogenation-induced charge transfer. Among XGnPs, edge-iodinated graphene nanoplatelets (IGnPs) exhibited remarkable electrocatalytic activities toward ORR with excellent long-term cycle stability in an alkaline medium. Although carbon-based electrocatalysts have demonstrated notably enhanced catalytic activities for ORR, they still struggle with poor stability during the OER process.[14]

Therefore, to improve the overall energy efficiency and retain the stability of the catalysts, efficient oxygen evolution is required. Transition metal oxides, such as spinel, pyrochlores, and perovskites, have been suggested as potential alternatives to noble metal-based OER catalysts.[15–19] Among them, perovskite oxides with the general formula of ABO_3 (the A-site is a rare and alkaline earth metal cation and the B-site is a 3d transition metal cation) have been extensively explored due to their unique structural and electronic properties. Following the report by Shao-Horn's group on perovskite catalysts for OER using σ* antibonding orbital occupation principles,[20] various perovskite oxides have been investigated as electrocatalysts for Li–air batteries, including $Sr_{0.95}Ce_{0.05}CoO_{3-\delta}$,[6] $Sr_2MMoO_{6-\delta}$,[21] $La_{0.8}Sr_{0.2}MnO_{3-\delta}$,[22] and $La_{0.6}Sr_{0.4}Co_{0.8}Fe_{0.2}O_{3-\delta}$.[23] The relatively sluggish ORR kinetics of

[a]Department of Energy Engineering, Ulsan National Institute of Science and Technology (UNIST), Ulsan, 44919, Republic of Korea. E-mail: ywju@unist.ac.kr; jbbaek@unist.ac.kr; gtkim@unist.ac.kr

[b]Department of Mechanical Engineering, Dong-Eui University, Busan, 47227, Republic of Korea

† Electronic supplementary information (ESI) available. See DOI: 10.1039/c5ta08493h

these perovskite oxides, however, necessitates proper support materials such as carbon. Thus, many studies have been carried out to grow or attach nanostructured oxide catalysts on carbon.[24,25] Notwithstanding these efforts, the *in situ* synthesis of perovskite oxides with a carbon support is still limited by their high sintering temperature.

With this background, we designed a new composite catalyst with excellent bifunctional activities toward both ORR and OER consisting of a nanorod type $Nd_{0.5}Sr_{0.5}CoO_{3-\delta}$ (NSC) perovskite and IGnPs *via* a simple ultrasonication method. Interestingly, the morphology of the composite was characterized by cloud-like IGnPs surrounding NSC nanorods. Since intermediation-spin Co(III) ions on the surface of the cobaltates offer an e_g^1 configuration,[20,26] the NSC nanorod perovskite exhibits superior OER activity. Moreover, IGnPs provide favorable binding affinity with O_2 molecules and fast electron transfer pathways,[13] contributing to dramatic improvement of the ORR performance. With these favorable properties, we investigated, for the first time, cloud-like IGnPs on NSC nanorods (NSC@IGnP) with excellent bifunctional activities toward both ORR and OER, remarkable cell performance, and exceptionally high stability for hybrid Li–air batteries.

Experimental

Preparation of IGnP, NSC, and the NSC@IGnP composite

Edge-iodinated nanoplatelets (IGnPs) were prepared by ball-milling the pristine graphite flake in a planetary ball-mill machine (Pulverisette 6, Fritsch) in the presence of iodine (I_2). The pristine graphite (5.0 g, Alfa Aesar, natural graphite, 100 mesh (<150 μm), 99.9995% metals basis, Lot #14735) was placed into a stainless steel ball-mill capsule (500 mL) containing stainless steel balls (500.0 g, diameter 5 mm). The capsule was sealed and degassed by five cycles of charging and discharging argon after applying reduced pressure (0.05 mmHg). Thereafter, I_2 gas was charged through a gas inlet with a cylinder pressure of 8.75 atm. The capsule was then fixed in the planetary ball-mill machine, and agitated with 500 rpm for 48 h. The resultant product was Soxhlet extracted with methanol to get rid of small molar mass organic impurities and 1 M aq. HCl solution to remove metallic impurities, if any. The final product was then freeze-dried at −120 °C under a reduced pressure (0.05 mmHg) for 48 h to yield 6.86 g (IGnPs have at least 1.86 g of I uptake).

A nanorod type $Nd_{0.5}Sr_{0.5}CoO_{3-\delta}$ (NSC) perovskite was prepared by the electrospinning method using a 15 wt% polyvinylpyrrolidone (PVP, average $M_w \sim 1\,300\,000$ by LS, Sigma-Aldrich Co.) solution of 0.1 M metal nitrate precursors in *N*,*N*-dimethylformamide (DMF, Alfa Aesar Co.). The metal nitrate solution was prepared by dispersing stoichiometric amounts of $Nd(NO_3)\cdot 6H_2O$ (Sigma-Aldrich Co., 99.9%, metal basis), $Sr(NO_3)_2$ (Sigma-Aldrich Co., 99+%), and $Co(NO_3)_2\cdot 6H_2O$ (Sigma-Aldrich Co., 98+%) in DMF solvent under continuous stirring. The prepared 15 wt% PVP metal nitrate solution was placed in a 30 mL syringe with a capillary tip ($D = 0.5$ mm). A variable high voltage power supply (Korea switching Co.) was used for the electrospinning process. The anode of the high voltage power supply was clamped to a syringe needle tip, and the cathode was connected to an aluminum foil collector. The applied voltage was 15 kV, the distance between the nozzle and collector was 15 cm, and the supply rate of the solution was 0.5 mL h^{-1}. The electrospun fibers were collected and sintered by heating to 850 °C at a rate of 2 °C min^{-1} in air, and holding them at that temperature for 4 h. The mass ratio of NSC to IGnPs was 1 : 1, 2 : 1, and 3 : 1 and each sample was denominated as NSC@IGnP (1 : 1), NSC@IGnP (2 : 1), NSC@IGnP (3 : 1), respectively. Each composite was dispersed in isopropyl alcohol (IPA) followed by a treatment of ultrasound with a 500 W ultrasonic generator for 1 h. The resultant product was then vacuum filtered followed by an overnight drying at 80 °C. Details of the electrochemical characterization with different mass ratios of NSC to IGnPs are available in the ESI (Fig. S7, ESI†). In this study, NSC@IGnP (2 : 1) was chosen as the optimized ratio and representatively named NSC@IGnP.

Characterization and electrochemical measurements on a half cell

The microstructure of the nanostructured materials was examined by scanning electron microscopy (SEM, Nova FE-SEM). The transmission electron microscopy (TEM) images were obtained using a high resolution-TEM (JEOL, JEM-2100F). The structure of NSC nanorods was characterized by using X-ray powder diffraction (XRD) (Rigaku diffractometer, Cu Kα radiation) with a scan rate of 0.5° min^{-1}. The powder pattern and lattice parameters were analyzed by Rietveld refinement using the GSAS program.

The electrochemical tests were carried out using a computer-controlled potentiostat (Biologic VMP3) with a RRDE-3A rotating disk electrode system. A platinum wire was used as the counter-electrode and an Hg/HgO (1 M NaOH filled) electrode as the reference electrode. The working electrodes were prepared by applying each of the catalyst inks onto a pre-polished glassy carbon disk electrode. The catalysts were first dispersed in ethanol/isopropyl alcohol solution (10 mg mL^{-1}) and Nafion (25 wt%) stock solution (10 μL) in ethanol was added to the catalyst ink by bath sonication to prepare the catalyst ink. The addition of a small amount of Nafion could effectively improve the dispersion of catalyst suspension and enhance the binding onto the GC electrode. A total of 5 μL well-dispersed catalyst ink was applied onto the prepolished glassy carbon (GC) disk electrode (5 mm in diameter).

The carefully prepared electrodes were dried at room temperature before the electrochemical tests. The number of electrons transferred (n) and peroxide yields (%) were calculated by the followed equations.[27,28]

$$n = 4 \times \frac{I_d}{I_d + I_r/N}$$

$$\%\ HO_2^- = 200 \times \frac{I_r/N}{I_d + I_r/N}$$

where I_d is the disk current, I_r is the ring current and N is the current collection efficiency of the Pt ring. N was experimentally determined to be 0.41 from the reduction of $K_3Fe[CN]_6$.

Preparation and assembly of a hybrid Li–air battery

A lithium foil with a thickness of 0.2 mm was obtained from Honjo metal, and disks with a diameter of 1 cm were cut for use as the anode. 1 M lithium hexafluorophosphate ($LiPF_6$, Sigma-Aldrich Co.) in tetraethylene glycol dimethyl ether (TEGDME, Sigma-Aldrich Co.) was used as an organic liquid electrolyte, and 0.1 M lithium hydroxide (LiOH, Sigma-Aldrich Co.) in pure water was used as the aqueous liquid electrolyte. The anode and cathode were separated by a $Li_{1+x+y}Ti_{2-x}Al_xP_{3-y}Si_yO_{12}$ (0.15 mm thickness, OHARA Inc., Japan) solid Li-ion conducting ceramic glass. The air electrodes were prepared by spraying the catalyst ink made using the prepared catalysts and PVdF–HFP binder (Sigma-Aldrich Co.) onto the gas-diffusion layer (Toray TGP-H-090). The catalyst loading density and binder content in the air electrode were 1 mg cm^{-2} and 20 wt%, respectively. Thus, current density could be easily normalized with the loading density of the catalyst (0.8 mg cm^{-2}). Details of the tested hybrid Li–air battery are available in the ESI.†

Results and discussion

A nanorod type $Nd_{0.5}Sr_{0.5}CoO_{3-\delta}$ (NSC) perovskite was synthesized by electrospinning metal nitrate precursors followed by subsequent calcination in air. Fig. S2a† presents a SEM image of the electrospun nanofibers with the homogeneous feature of an average diameter of around 300 nm. NSC nanorods, with an average diameter of 150 nm, are formed after thermal decomposition of PVP upon calcination at 850 °C for 4 h in air (Fig. S2b, ESI†). The transmission electron microscopy (TEM) image also confirms the nanorod type NSC (Fig. 1a) and energy-dispersive X-ray spectroscopy (EDS) shows a corresponding elemental analysis of the NSC nanorods (Fig. 1b). The EDS images of the NSC nanorod indicate that all elements are uniformly distributed throughout the perovskite nanorod. Fig. 1c presents a high resolution TEM (HR-TEM) image with the selected area electron diffraction (SAED) pattern of the prepared sample, indicating that the NSC nanorod has high crystallinity. To identify the crystalline structure of the NSC nanorod, X-ray diffraction (XRD) patterns with Rietveld refinement are analyzed (Fig. 1d). The observed diffraction peaks can be indexed to perovskite structures without any detectable impurities.[29] The lattice parameters are $a = 5.837$ Å, $b = 5.433$ Å, and $c = 7.617$ Å, indicating that the NSC nanorod can be indexed to a space group of *Pnma*.

Fig. 2a shows a TEM image with the schematic illustration of edge-iodinated graphene nanoplatelets on the NSC nanorod (NSC@IGnP). Interestingly, the simple method of ultrasonication leads to NSC@IGnP having a fascinating morphology with cloud-like graphene platelets around NSC nanorods. The typical thickness of the IGnP layers covering NSC was approximately 10 nm. Recently, high energy wet-milling has been explored to fabricate graphitic layer coated metal-oxides.[30,31] Surface graphitic layers on metal-oxides can provide facile electron conductive pathways and an extended electrochemically active area toward the ORR process.[30,31] Suslick reported that ultrasound delivers extremely high energy during interparticle collisions at the liquid–solid interface,[32] which could explain the formation of the IGnP layers throughout the NSC nanorod by ultrasonication in this study. Furthermore, an EDS analysis was carried out to reveal the elemental profiles of the NSC@IGnP, which confirms that IGnPs uniformly cover NSC nanorods (Fig. 2b).

The oxygen reduction activities of Pt/C, NSC, IGnP, and NSC@IGnP were investigated by rotating ring disk electrode (RRDE) experiments in O_2-saturated 0.1 M LiOH. Fig. 3a shows the ORR performance of each sample by linear sweep voltammetry (LSV) measurement on the RRDE at a rotation rate of 1600 rpm and a scan rate of 0.01 V s^{-1}. The onset potential for oxygen reduction of IGnPs is −0.09 V *versus* a Hg/HgO reference electrode, which is slightly higher than that of Pt/C (+0.05 V). Meanwhile, the limiting current of IGnPs is even higher than that

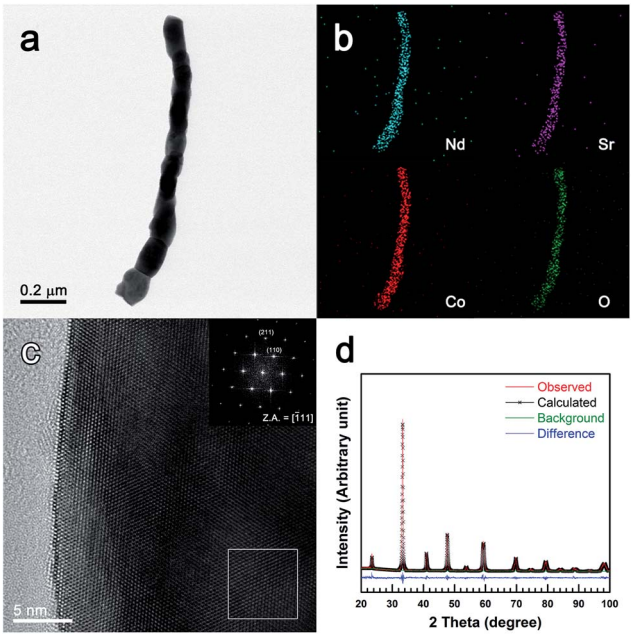

Fig. 1 (a) Bright-field (BF) TEM image of a NSC nanorod, (b) elemental mapping by EDS from TEM, (c) a high-resolution (HR) TEM image of a NSC nanorod and the selected area electron diffraction (SAED) pattern shown as the inset, and (d) XRD patterns of the NSC nanorod.

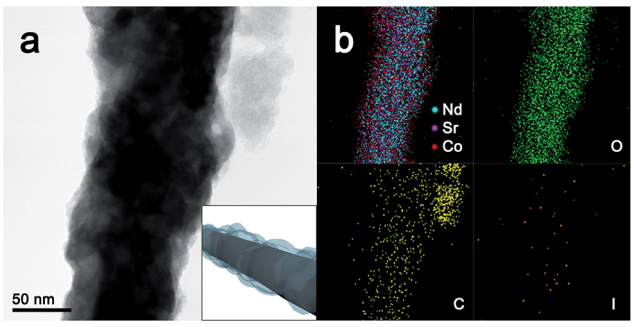

Fig. 2 (a) TEM image of NSC@IGnP with the schematic illustration as the inset. (b) Elemental mapping by EDS from TEM energy-filtered images.

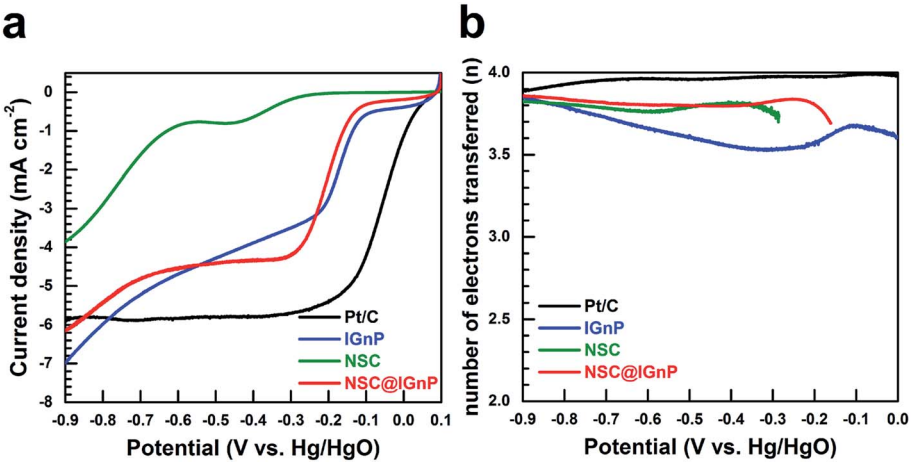

Fig. 3 (a) ORR polarization curves of Pt/C, IGnPs, NSC, and NSC@IGnP, respectively, in O_2-saturated 0.1 M LiOH at a rotation rate of 1600 rpm and a scan rate of 0.01 V s^{-1} and (b) the number of electrons transferred (n).

of Pt/C at the higher overpotential area, revealing exceptional ORR activity of IGnPs, as reported.[13] While only NSC shows a relatively high onset potential with low current density, the composite of NSC@IGnP presents dramatically enhanced ORR activities, contributed by IGnPs, offering favorable O_2 molecule binding affinity along with weakened O–O bond strength.[13]

To obtain further insight into electrocatalytic pathways for ORR, the number of electrons transferred (n) and the peroxide yields (%) of the samples were calculated from the disk (Fig. 3a) and ring currents (Fig. S3a, ESI†) on a rotational disk-ring electrode. The number of electrons transferred (n) at −0.8 V for IGnPs, NSC, and NSC@IGnP was determined to be 3.83, 3.74, and 3.80, respectively (Fig. 3b). The corresponding peroxide yields (%) were measured to be less than 10% (Fig. S3b, ESI†), suggesting a predominant four-electron transfer pathway during the ORR process. These results reveal that the composite of NSC@IGnP is a highly promising electrocatalyst in an alkaline solution due to its excellent ORR activity and cost-effectiveness compared to the benchmark Pt/C catalyst.

Furthermore, efficient oxygen evolution is required to achieve higher energy efficiency and retain the stability of the catalysts. The activities of the oxygen evolution reaction (OER) were measured in O_2-saturated 0.1 M LiOH at a rotation rate of 1600 rpm and a scan rate of 0.01 V s^{-1}. Fig. 4a shows the polarization curves of OER after ten consecutive polarization scans for IGnPs, NSC, and NSC@IGnP, and IrO_2 as a reference. IGnPs present very poor OER electrocatalytic activity with a high onset potential and a low current density. On the other hand, NSC shows excellent OER activity, outperforming IrO_2 because the intermediate-spin Co(III) cations on the surface provide an e_g^1 configuration.[20,26] Moreover, OER activities are notably enhanced for the NSC@IGnP, as confirmed by the much lower onset potential and higher current density. The synergistic OER enhancement of NSC@IGnP could stem from the high OER activity of NSC and the efficient electron transfer pathways of uniformly coated IGnPs. Fig. 4b displays the current densities along ten consequent scans at 0.9 V for each electrocatalyst. For the first scan, IGnPs exhibit an onset potential of 0.35 V and a current density of

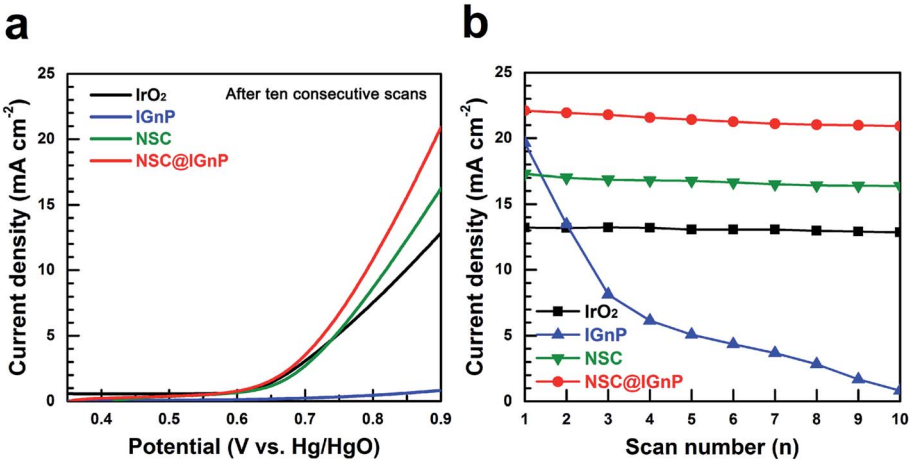

Fig. 4 (a) OER polarization curves after ten consecutive scans for IrO_2, IGnPs, NSC, and NSC@IGnP, respectively, in O_2-saturated 0.1 M LiOH at a rotation rate of 1600 rpm and a scan rate of 0.01 V s^{-1} and (b) current densities along ten consequent scans at 0.9 V.

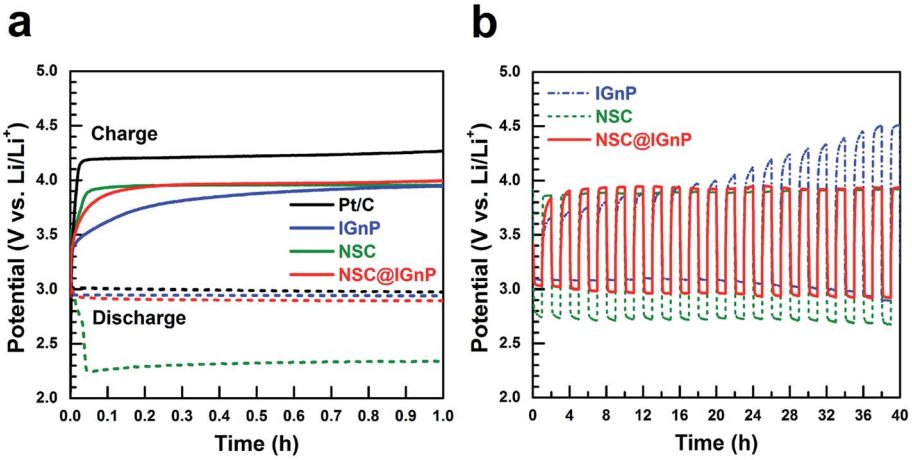

Fig. 5 (a) First discharge–charge curves of Pt/C, IGnPs, NSC, and NSC@IGnP, respectively, in 0.1 M LiOH at a current density of 625 mA g^{-1} and (b) cycling performance at a current density of 125 mA g^{-1} for IGnPs, NSC, and NSC@IGnP.

19.6 mA cm^{-2} at 0.9 V, whose value is superior to that of IrO_2 (Fig. S4, ESI†). In contrast, severe degradation of the OER performance is observed during ten consecutive scans for IGnPs, resulting in a positive shift of the onset potential and a significant drop of the current density. These results confirm that IGnPs are highly vulnerable to the OER process, as generally observed for carbon-based materials,[14] while NSC shows highly efficient OER activities without degradation during ten consecutive scans. Interestingly, the composite NSC@IGnP exhibits highly stable and superior OER activities, possibly originating from OER catalytic properties of NSC. This suggests that NSC@IGnP is a prospective OER catalyst, providing remarkable performance with high durability in alkaline media.

The electrochemical performance of Pt/C, IGnPs, NSC, and NSC@IGnP was evaluated using a hybrid Li–air battery. Fig. 5a shows the first discharge–charge curves of Pt/C, IGnPs, NSC, and NSC@IGnP in 0.1 M LiOH at a current density of 625 mA g^{-1}. The discharge voltage plateaus are obtained at 2.98, 2.94, 2.33, and 2.89 V *versus* Li/Li^+ for Pt/C, IGnPs, NSC, and NSC@IGnP, respectively. More discharge profiles are investigated at higher current densities in the range of 625 to 2500 mA g^{-1} (Fig. S5, ESI†). At 625 mA g^{-1}, the discharge voltage of NSC@IGnP is only 0.09 V lower than that of Pt/C. Even at a higher current density of 2500 mA g^{-1}, the difference in the discharge voltage between NSC@IGnP and Pt/C is only 0.1 V. These results demonstrate that the NSC@IGnP catalyst is comparable to Pt/C even in the high current density region. Fig. 5b presents the cycling performance of IGnPs, NSC, and NSC@IGnP at a constant current density of 125 mA g^{-1} in ambient air. IGnPs show obvious degradation during 40 h with a substantial increase in the discharge–charge voltage gap from 0.58 V to 1.62 V. This result is in accordance with the vulnerability of IGnPs during the OER process (Fig. S4, ESI†). For NSC, in contrast, invariant cycling performance was obtained during 40 h more reduced charge overpotential relative to IGnPs. However, the relatively sluggish ORR kinetics of NSC causes a low discharge performance with a high discharge–charge voltage gap of 1.23 V. In the case of NSC@IGnP, outstanding cycling performance was obtained during 40 h with the lowest discharge–charge voltage gap (less than 1.0 V). Consequently, NSC@IGnP is an efficient bifunctional catalyst with comparable performance to noble metal based catalysts, such as Pt/C and IrO_2, for a hybrid Li–air battery.

Conclusion

In summary, we have fabricated cloud-like IGnPs on NSC nanorods (NSC@IGnP) as a bifunctional catalyst for both ORR and OER *via* a simple ultrasonication method. We demonstrated that NSC nanorods are an efficient and durable catalyst for OER, outperforming IrO_2. A composite with the IGnPs achieved significantly improved ORR activities, including dramatically increased current density and enhanced onset potential. Moreover, benefiting from the unique morphological features, NSC@IGnP presents vastly superior OER activity over NSC only, stemming from the facile electron conductive pathways of the surface graphitic layers. Evaluation with a hybrid Li–air battery confirmed that NSC@IGnP is a highly promising bifunctional electrocatalyst with comparable performance and cost-effectiveness to the benchmark Pt/C and IrO_2 catalysts in alkaline media.

Acknowledgements

This research was supported by the Mid-career Researcher Program (NRF-2013R1A2A2A04015706, NRF-2015R1A2A1A10055886) and the Creative Research Initiative (CRI) Program through the National Research Foundation of Korea, funded by the Ministry of Science, ICT and Future Planning. It was also supported by the 2015 Research Fund (1.150120.01) of UNIST (Ulsan National Institute of Science & Technology).

References

1 K. M. Abraham and Z. Jiang, *J. Electrochem. Soc.*, 1996, **143**, 1–5.

2 G. Girishkumar, B. McCloskey, A. C. Luntz, S. Swanson and W. Wilcke, *J. Phys. Chem. Lett.*, 2010, **1**, 2193–2203.
3 B. Kumar, J. Kumar, R. Leese, J. P. Fellner, S. J. Rodrigues and K. M. Abraham, *J. Electrochem. Soc.*, 2010, **157**, A50–A54.
4 J.-S. Lee, S. T. Kim, R. Cao, N.-S. Choi, M. Liu, K. T. Lee and J. Cho, *Adv. Energy Mater.*, 2011, **1**, 34–50.
5 J. Christensen, P. Albertus, R. S. Sanchez-Carrera, T. Lohmann, B. Kozinsky, R. Liedtke, J. Ahmed and A. Kojic, *J. Electrochem. Soc.*, 2012, **159**, R1–R30.
6 W. Yang, J. Salim, S. Li, C. Sun, L. Chen, J. B. Goodenough and Y. Kim, *J. Mater. Chem.*, 2012, **22**, 18902–18907.
7 E. Yoo and H. Zhou, *RSC Adv.*, 2014, **4**, 11798–11801.
8 H. Peng, Z. Mo, S. Liao, H. Liang, L. Yang, F. Luo, H. Song, Y. Zhong and B. Zhang, *Sci. Rep.*, 2013, **3**, 1765–1771.
9 D. Liu, X. Zhang, Z. Sun and T. You, *Nanoscale*, 2013, **5**, 9528–9531.
10 Y. Zhang, K. Fugane, T. Mori, L. Niu and J. Ye, *J. Mater. Chem.*, 2012, **22**, 6575–6580.
11 Z.-H. Sheng, H.-L. Gao, W.-J. Bao, F.-B. Wang and X.-H. Xia, *J. Mater. Chem.*, 2012, **22**, 390–395.
12 Y.-W. Ju, S. Yoo, C. Kim, S. Kim, I.-Y. Jeon, J. Shin, J.-B. Baek and G. Kim, *Adv. Sci.*, 2016, **3**, 1500205–1500209.
13 I.-Y. Jeon, H.-J. Choi, M. Choi, J.-M. Seo, S.-M. Jung, M.-J. Kim, S. Zhang, L. Zhang, Z. Xia, L. Dai, N. Park and J.-B. Baek, *Sci. Rep.*, 2013, **3**, 1810–1816.
14 L. Li and A. Manthiram, *Adv. Energy Mater.*, 2014, **4**, 1301795–1301801.
15 J.-I. Jung, M. Risch, S. Park, M. G. Kim, G. Nam, H.-Y. Jeong, Y. Shao-Horn and J. Cho, *Energy Environ. Sci.*, 2016, **9**, 176–183.
16 S. H. Oh, R. Black, E. Pomerantseva, J.-H. Lee and L. F. Nazar, *Nat. Chem.*, 2012, **4**, 1004–1010.
17 J. Parrondo, M. George, C. Capuano, K. E. Ayers and V. Ramani, *J. Mater. Chem. A.*, 2015, **3**, 10819–10828.
18 J.-I. Jung, H. Y. Jeong, J.-S. Lee, M. G. Kim and J. Cho, *Angew. Chem.*, 2014, **126**, 4670–4674.
19 H.-Y. Wang, Y.-Y. Hsu, R. Chen, T.-S. Chan, H. M. Chen and B. Liu, *Adv. Energy Mater.*, 2015, 1500091–1500098.
20 J. Suntivich, K. J. May, H. A. Gasteiger, J. B. Goodenough and Y. Shao-Horn, *Science*, 2011, **334**, 1383–1385.
21 M. Cheriti and A. Kahoul, *Mater. Res. Bull.*, 2012, **47**, 135–141.
22 C. Jin, X. Cao, L. Zhang, C. Zhang and R. Yang, *J. Power Sources*, 2013, **241**, 225–230.
23 E. M. Garcia, H. A. Tarôco, T. Matencio, R. Z. Domingues and J. A. F. D. Santos, *Int. J. Hydrogen Energy*, 2012, **37**, 6400–6406.
24 G. Nam, J. Park, M. Choi, P. Oh, S. Park, M. G. Kim, N. Park, J. Cho and J.-S. Lee, *ACS Nano*, 2015, **9**, 6493–6501.
25 M. Prabu, P. Ramakrishnan, P. Ganesan, A. Manthiram and S. Shanmugam, *Nano Energy*, 2015, **15**, 92–103.
26 J. O. 'M. Bockris and T. Otagawa, *J. Electrochem. Soc.*, 1984, **131**, 290–302.
27 U. A. Paulus, T. J. Schmidit, H. A. Gasteiger and R. J. Behm, *J. Electroanal. Chem.*, 2001, **495**, 134–145.
28 Y. Liang, Y. Li, H. Wang, J. Zhou, J. Wang, T. Reiger and H. Dai, *Nat. Mater.*, 2011, **10**, 780–786.
29 S. Choi, J. Shin, K. M. Ok and G. Kim, *Electrochim. Acta*, 2012, **81**, 217–223.
30 H. K. Noh, H.-S. Park, H. Y. Jeong, S. U. Lee and H.-K. Song, *Angew. Chem.*, 2014, **126**, 5159–5163.
31 X. Zhou, X. Liu, Y. Xu, Y. Liu, Z. Dai and J. Bao, *J. Phys. Chem. C*, 2014, **118**, 23527–23534.
32 K. S. Suslick, *Science*, 1990, **247**, 1438–1445.